Superconductor
Science and
Technology

PAPER • **OPEN ACCESS**

Numerical and experimental investigation of AC losses in MgB_2 wires

To cite this article: L Soldati *et al* 2025 *Supercond. Sci. Technol.* **38** 065019

OPEN ACCESS
IOP Publishing
Superconductor Science and Technology
Supercond. Sci. Technol. **38** (2025) 065019 (19pp)
https://doi.org/10.1088/1361-6668/addd88

Numerical and experimental investigation of AC losses in MgB_2 wires

L Soldati[1,*], J Dular[2], J Kovac[3], P Kovac[3], M Cialone[1,4], T Spina[5], C-E Bruzek[5], M Wozniak[2], M Putti[1,4] and M Breschi[6]

[1] Department of Physics, Università di Genova, Genova, Italy
[2] CERN, Geneva, Switzerland
[3] Institute of Electrical Engineering of SAS, Bratislava, Slovakia
[4] CNR-SPIN, Genova, Italy
[5] ASG Superconductors S.p.a., Genova, Italy
[6] Department of Electrical, Electronic and Information Engineering, Università di Bologna, Bologna, Italy

E-mail: luca.soldati94@gmail.com

Received 21 November 2024, revised 1 April 2025
Accepted for publication 20 May 2025
Published 12 June 2025

Abstract

The efficacy of MgB_2-based cables for DC power transmission applications is well-established due to several advantageous properties such as the natural abundance and cost-effectiveness of precursor powders and the innate compatibility with liquid hydrogen, which has a boiling point of 20 K. Notably, MgB_2 has a critical temperature T_c of 39 K. However, transitioning this technology to alternating current (AC) applications, like electric motors or AC power transmission, poses challenges primarily due to the material's susceptibility to AC losses when subjected to alternating fields. Therefore, it is crucial to conduct a thorough investigation into the dissipative phenomena affecting MgB_2 wires under AC conditions to develop design strategies for optimizing these wires for such applications. A detailed study involving both numerical simulations and experimental analyses has been conducted to understand the complex electrodynamics of MgB_2 wires under sinusoidal time-varying external field conditions. Remarkably, a comprehensive numerical model has been developed, incorporating all dissipative contributions in a multifilamentary wire in a single numerical tool. This model also includes the ferromagnetic loss contributions due to the presence of ferromagnetic materials like Nickel and Monel in the stabilizing matrix. The monolithic nature of this model allows for a general treatment of AC losses in multifilamentary wires, accounting for the influence of ferromagnetic materials within the stabilizing matrix.

Keywords: AC losses, FEM, MgB_2

* Author to whom any correspondence should be addressed.

1. Introduction

The accurate simulation of alternating current (AC) losses in multifilamentary wires remains a significant challenge for the superconductors modeling community [1–4]. This complexity arises from the intricate three-dimensional (3D) geometries, nonlinear superconducting (SC) properties-often described by the power-law relation for resistivity [5]-and the need to analyze these systems under dynamic, time-varying conditions [6–8]. These aspects are critical when examining dissipative losses under AC conditions [9, 10]. Among various methodologies, the *eddy-current* modeling approach has proven to be particularly effective [11–13].

Replicating the nonlinear phenomena in a time-dependent scenario, especially within the high aspect-ratio geometry of multifilamentary wires, presents significant challenges. The disparity between the full twist pitch length and the wire's transverse dimension requires a dense mesh discretization, imposing substantial computational demands. This requirement is particularly taxing when using a 3D Finite Element Method (3D FEM), known for its effectiveness in solving eddy-current problems in superconducting wires [1, 14, 15].

To alleviate the computational burden of a 3D 'brute-force' approach, which involves modeling at least one full twist pitch length and discretizing the entire geometry, various alternative strategies have been developed. One approach involves analyzing the geometric patterns typical of multifilamentary wire designs, such as helices [9, 16], though effective only for simplified cases [17–19]. Another strategy applies specific periodic boundary conditions to reduce the problem's dimensions from the total twist length to a fraction thereof [20]. Additionally, homogenization techniques can be applied to simplify the bundle of filaments [21], while nonlinear circuit models, using lumped circuit elements evaluated through preliminary FE analyses, were also proposed in [22]. Despite these efforts, the complexity often remains high, involving from hundreds of thousands to millions of Degrees of Freedom. Without cluster or parallel computing resources [23], the computational demand becomes prohibitively high for standard workstations, rendering it unsuitable for parametric or geometric optimization studies, which require relatively quick simulations.

The computational complexity is further exacerbated in MgB_2-based SC wires [24] due to their material-specific characteristics [25, 26]. During the mechanical and thermal treatments required for wire fabrication using the *ex-situ* Powder-In-Tube (PIT) technique, the MgB_2 powders and the resistive matrix are subjected to heating, which can lead to the formation of secondary phases that degrade the wire's SC properties. Therefore, it is crucial to select an outer sheath material that exhibits minimal reactivity with the powders. Additionally, the sheath must possess suitable mechanical properties to efficiently transfer processing-induced mechanical stress to the SC powders [26, 27]. Balancing these requirements, nickel is chosen as the sheath material despite its ferromagnetic nature, which increases computational complexity and poses challenges for iterative solvers.

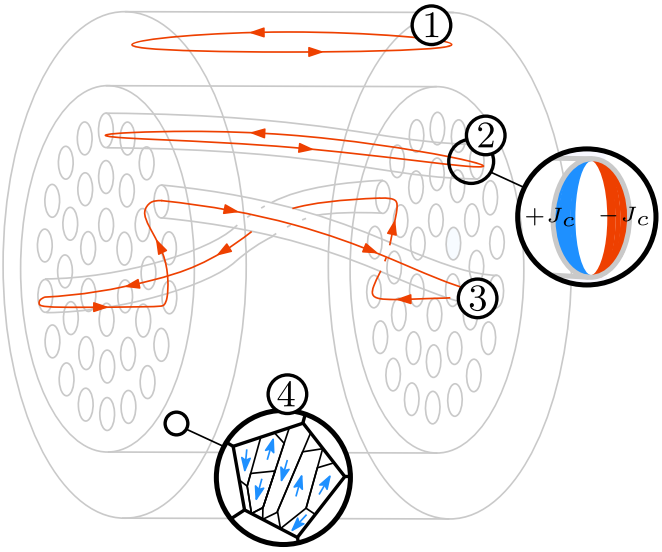

Figure 1. Illustration of various loss contributions in a multifilamentary MgB_2 wire. (1) Eddy currents caused by parasitic effects in the resistive matrix. (2) Screening currents in the superconducting filaments, modeled using the critical state model (CSM). (3) Coupling currents flowing between adjacent filaments. (4) Ferromagnetic hysteresis, highlighting the magnetic domains in the ferromagnetic stabilizing matrix material. The hysteresis loop defined by the $B(H)$ curve indicates energy dissipation as heat.

To elucidate the different types of dissipative contributions to total losses in a multifilamentary MgB_2 wire, we outline the following categories, as shown in figure 1:

(i) *Eddy Current Losses*. Localized losses occurring within the resistive material of the stabilizing matrix, arising from currents originating and circulating within the matrix, resulting in dissipative effects.
(ii) *SC Hysteretic Losses*. Dissipation resulting from the penetration and movement of magnetic flux within the material, caused by time-varying operational conditions, such as fluctuating transport currents and external magnetic fields.
(iii) *Coupling Current Losses*. Losses within the resistive matrix of the material, stemming from currents transitioning between distinct SC filaments, inducing effective coupling and leading to dissipation.
(iv) *Ferromagnetic Hysteretic Losses*. Dissipation associated with the magnetization loops in ferromagnetic materials exhibiting hysteretic behavior. The area enclosed by a $B(H)$ closed loop represents the energy irreversibly dissipated in the material as heat.

This study aims to elucidate the contributions of various loss mechanisms in a multifilamentary MgB_2 wire and their cumulative impact on total losses. Additionally, it seeks to develop an efficient numerical tool for calculating losses in a multifilamentary wire subjected to time-varying transport currents and time-varying external magnetic fields, within a time frame conducive to parametric and optimization studies.

Ideally, this numerical tool would complete simulations within minutes rather than hours or days.

In section 2, we present the numerical framework developed to address the problem of AC losses in multifilamentary MgB_2 wires. This framework is based on an advanced modeling approach that comprehensively accounts for all loss contributions within the wire, as illustrated in figure 1. Numerical computations were performed using GetDP [28], with geometries and meshes generated using Gmsh [29]. All the software is open-source. Section 2.2 describes the approach to the classical magnetodynamic problem using an eddy-current model, leveraging the symmetric geometry of the wires to reduce computational complexity (reduced-order FE model). In section 2.3, we detail the model component that calculates the hysteretic ferromagnetic losses due to Nickel and Monel in the stabilizing matrices of the wires. In section 3, we describe the design of multifilamentary MgB_2 wires produced by the *Strategic Business Unit SC Materials* of ASG Superconductors, which were analyzed in this study. In section 4, we elaborate on the measurement system and the testing campaign, detailing the setup and procedures to provide insight into the unique methodology adopted in this study.

2. Modeling framework

This section details the computational framework developed to analyze AC losses within multifilamentary MgB_2 wires in the presence of ferromagnetic matrices. As alluded to in section 1, a classical 3D FEM-based eddy-current model proves inadequate for capturing all the dissipative contributions occurring within wires comprised of magnetic materials. Further development is required to calculate the contribution of ferromagnetic hysteresis losses (contribution (iv) in figure 1) to the total losses.

The proposed approach builds on prior studies [30, 31] demonstrating the feasibility of addressing electrodynamic and hysteretic-ferromagnetic problems with tailored methodologies. In this work, these aspects are integrated into a unified, monolithic framework, where coupling currents and ferromagnetic losses are jointly accounted for. Although detailed in separate subsections for clarity, these contributions are fully coupled and solved simultaneously within a single computational model.

In section 2.1, we will examine how the geometry of the problem can be leveraged to facilitate its simplification into a reduced-order FEM model. In section 2.2 an eddy-current formulation will be employed to depict a relatively standard magnetodynamic problem for superconductors, thereby representing contributions (i), (ii), and (iii) in figure 1. In section 2.3, to account for the ferromagnetic hysteretic behavior of Nickel and Monel, an alternative formulation will be employed. The latter will then be used to compute the dissipative contribution arising from the hysteretic ferromagnetic materials, thereby modeling contribution (iv), as identified in figure 1.

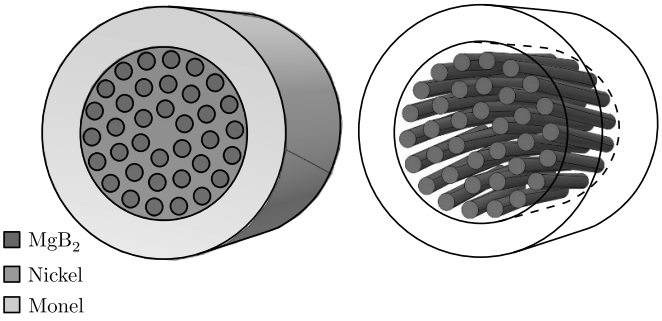

Figure 2. The figure depicts a cross-section of a multifilamentary wire used in this study, identifying the three constituent materials of the wires commercialized by ASG Superconductors. These materials include *ex-situ* processed MgB_2 filaments, a Nickel matrix, and an outer metallic sheath composed of Monel, a nickel-copper alloy.

2.1. About helices and periodic symmetries

This portion of the study highlights particular insights that arise when analyzing a 3D cross-sectional view of a multifilamentary wire. Within this cross-section, numerous filaments are arranged in a structural configuration established during the wire fabrication process. The *ex-situ* PIT method is utilized, wherein metallic tubes are filled with pre-reacted powders. These tubes are then assembled into billets and shaped to ensure a well-organized, uniform distribution of filaments.

Upon scrutinizing the arrangement of filaments within the wire bundle and matrix, a noticeable periodic pattern becomes evident in the 3D geometry. In wires possessing circular cross-sections, this periodic arrangement is accomplished through twisting during the manufacturing process, which takes place concurrently with the drawing process. Each filament experiences a rotation of 2π after one twist pitch length, resulting in a section returning to its initial position within the matrix after completing a full twist pitch, here denoted as p.

A well-defined symmetrical pattern dictates the organization of individual filaments within the stabilizing matrix. Importantly, traversing a full twist pitch along the wire's longitudinal axis is not necessary to return to a section exhibiting the same filament arrangement as the starting section. In cases where the filament organization within a specific cross-section exhibits periodicity, it is sufficient to traverse only a fraction of the total twist pitch before encountering a subsequent cross-section possessing the same filament arrangement as the initial section. As exemplified in figure 2, which depicts the wire design under investigation, a wire composed of 36 filaments exhibits a rotational symmetry of $\pi/3$ radians in the filament arrangement. This implies that the entire two-dimensional (2D) geometry of the section can be reconstructed by utilizing six identical and super-imposable wedges ($\frac{2\pi}{\pi/3} = 6$). In a scenario with periodicity of $\pi/3$, as in our case, an identical section is encountered after covering only $1/6$ of the twist pitch (denoted by $\ell = p/6$), as depicted in figure 3.

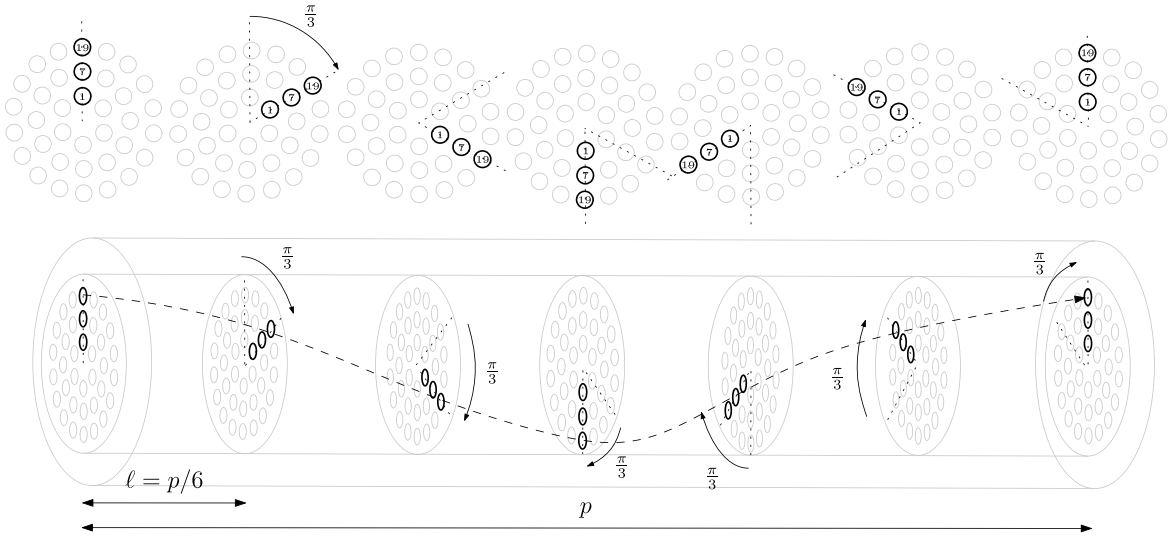

Figure 3. The image depicts a complete twist of the 36 filaments design wire analysed in this work. (b) It illustrates how the rotational speed, defined by the twist pitch, results in a configuration where the filaments, exhibiting a $s = \pi/3$ periodic symmetry, return to an identical positional arrangement after one $\frac{p}{2\pi/s}$ twist fraction. This identical arrangement is rotated by $\pi/3$ from the original reference. (a) Each 2D cross-section of the wire is highlighted individually.

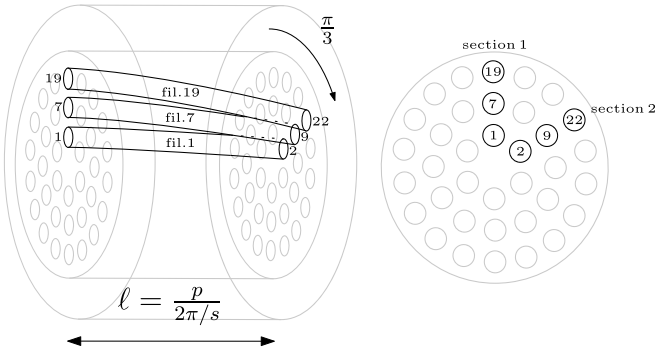

Figure 4. The image depicts a fraction of the total twist pitch. The represented length corresponds to the minimum distance over which the arrangement of the individual filaments in a cross-section becomes superimposable on the initial configuration (in a non-ordered manner). Following this logic, filaments 1, 7, and 19 (where the numbers are assigned based on the configuration given by the initial cross-section, section 1) assume the positions #2, #9, and #22 in the final cross-section (section 2).

While the filaments do not align with those in the starting section, they occupy positions adjacent to their original locations in the final section. After traversing a distance of ℓ in the z-direction, the position previously occupied by filament #1 in the starting section is now occupied by filament #2, figure 4.

The CATI method (*Coupled Axial and Transverse Currents Method*) [32], described in the next section, operates on the premise of cross-sectional periodicity along the wire's principal axis, represented here by the z-axis. In this context, the parameter ℓ denotes the periodicity length along z, indicating the distance after which each filament occupies the position of another filament, while maintaining the same filament arrangement as in the starting section. It is computed as a fraction of the twist length p using the relation $\ell = p/n$, where n denotes the number of equal wedges into which the wire section can be divided. In the depicted geometry, and in all geometries analyzed in this study, the minimum possible value of ℓ is $p/6$.

2.2. The CATI method

The CATI method [32] comprises two 2D models: one describing out-of-plane currents (along z-axis) and the associated transverse magnetic field, and another describing in-plane currents (perpendicular to z-axis), representing the coupling effect between filaments. These in the following text will be referred to as *Axial Current* (AI, the out-of-plane subpart of the model) and *Transversal Current* (TI, the in-plane subpart of the model) problems, respectively. Net currents and voltages are introduced for each model as global variables, and the AI and TI problems are coupled via these global quantities using circuit equations, as depicted in figure 5.

2.2.1. The AI—axial currents—problem. The AI model is governed by Maxwell's equations in the magnetodynamic (or magneto-quasistatic) regime [33], whose strong form reads

$$\begin{cases} \nabla \cdot \mathbf{B} = 0, \\ \nabla \times \mathbf{H} = \mathbf{J}_{\text{op}}, \\ \nabla \times \mathbf{E}_{\text{op}} = -\partial_t (\mathbf{B}), \end{cases} \tag{1}$$

where $\mathbf{B} = \mu \mathbf{H}$ is the magnetic flux density (T), $\mathbf{H}$ is the magnetic field (A m^{-1}), $\mathbf{J}_{\text{op}}$ is the current density (A m^{-2}), $\mathbf{E}_{\text{op}} = \rho \mathbf{J}_{\text{op}}$ is the electric field (V m^{-1}), μ is the permeability (H m^{-1}), and ρ is the resistivity (Ωm).

We define $\mathbf{J}_{\text{op}}$ and $\mathbf{E}_{\text{op}}$ as axial vectors, possessing only an out-of-plane vector component along the z-axis ($J_{\text{op}}\hat{k}$, $E_{\text{op}}\hat{k}$), where $\hat{k}$ is the unit vector along the z-axis. Conversely, $\mathbf{H}$ and $\mathbf{B}$ are defined as transverse vectors, confined to the in-plane

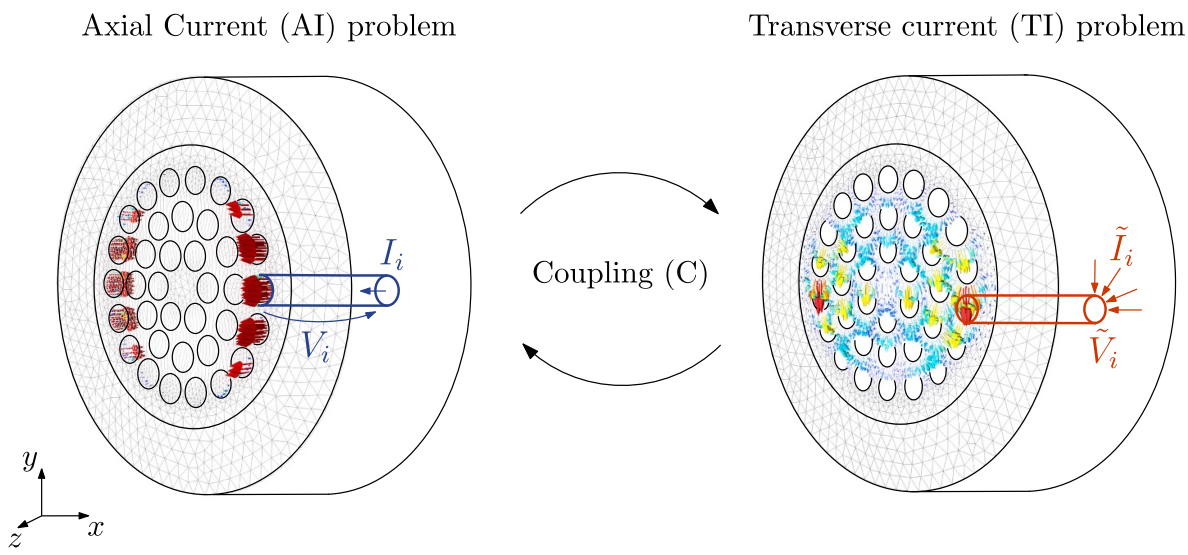

Figure 5. In the figure, the two 2D subproblems solved using the CATI formulation are depicted. On the left, the classical magnetodynamic subproblem is shown, representing the standard formulation typically used to approach the problem of AC losses. It solves for the transverse currents, flowing along z. On the right, the 2D electrodynamic subproblem is illustrated, which models the coupling currents, or transverse currents, flowing in the x–y plane.

dimensions and perpendicular to the z-axis ($H_{\mathrm{ip},x}\hat{i}$, $H_{\mathrm{ip},y}\hat{j}$), ($B_{\mathrm{ip},x}\hat{i}$, $B_{\mathrm{ip},y}\hat{j}$), where $\hat{i}$ and $\hat{j}$ are the unit vectors along the x- and y-axes, respectively. The chosen weak form of the model is that of a classical 2D $\mathbf{H}$-ϕ-formulation, in order to ensure numerical efficiency in the treatment of the superconductor power law for resistivity [6].

The weak form of the defined problem reads [32]

$$\int_{\Omega} \partial_t(\mu\mathbf{H})\cdot\mathbf{H}'\mathrm{d}\Omega + \int_{\Omega_c} \rho(\nabla\times\mathbf{H})\cdot(\nabla\times\mathbf{H}')\,\mathrm{d}\Omega_c = V_t\mathcal{I}_t(\mathbf{H}') + \sum_{i\in N_f} V_i\mathcal{I}_i(\mathbf{H}'), \tag{2}$$

where Ω represents the total simulation domain, and Ω_c denotes the conductive subdomain. The operator $\mathcal{I}_i(\mathbf{H})$ represents the circulation of $\mathbf{H}$ around filament $\Omega_{\mathrm{f},i}$, corresponding to the net current, denoted by I_i, flowing in filament $i \in N_f$, where N_f is the total number of filaments in the wire. The associated voltage is denoted by V_i. The operator $\mathcal{I}_t(\mathbf{H})$ is the net current flowing in the whole conductor, i.e. the transport current, denoted by I_t, which is the sum of the currents in all the filaments and in the conductor matrix.

2.2.2. The TI—transversal currents—problem. The TI model follows the electrodynamics equations for direct current (DC) flow [33], expressed as

$$\begin{cases} \nabla\cdot\mathbf{J}_{\mathrm{ip}} = 0, \\ \nabla\times\mathbf{E}_{\mathrm{ip}} = \mathbf{0}, \end{cases} \tag{3}$$

where $\mathbf{J}_{\mathrm{ip}} = \sigma\mathbf{E}_{\mathrm{ip}}$ represents the coupling current density (A m^{-2}), $\mathbf{E}_{\mathrm{ip}}$ denotes the coupling current electric field (V m^{-1}), and $\sigma = 1/\rho$ stands for electrical conductivity (S m^{-1}). The TI problem is addressed solely within the matrix, and both $\mathbf{J}_{\mathrm{ip}}$ and $\mathbf{E}_{\mathrm{ip}}$ are characterized as in-plane fields ($J_{\mathrm{ip},x}\hat{i}$,$J_{\mathrm{ip},y}\hat{j}$), ($E_{\mathrm{ip},x}\hat{i}$,$E_{\mathrm{ip},y}\hat{j}$).

The TI model translates the divergence-free condition on the current density $\mathbf{J}_{\mathrm{ip}}$ into a weak form. The current density is expressed as,

$$\mathbf{J}_{\mathrm{ip}} = -\sigma\nabla V, \tag{4}$$

with V a scalar potential defined such that $\mathbf{E} = -\nabla V$.

On the filament boundaries $\partial\Omega_{\mathrm{f},i}$, $i \in N_f$, we define

$$\widetilde{I}_i = \int_{\partial\Omega_{\mathrm{f},i}} \mathbf{J}_{\mathrm{ip}}\cdot\mathbf{n}\,\mathrm{d}S, \tag{5}$$

which represents the net current entering filament $i \in N_f$.

We represent the voltage $V|_{\partial\Omega_{\mathrm{f},i}} = \widetilde{V}_i$ for $i \in N_f$. Alongside their corresponding currents $\widetilde{I}_i$, these quantities represent the global variables of the TI problem. Considering the constant nature of V' on $\partial\Omega_{\mathrm{f},i}$, the weak form is presented as [32]

$$\int_{\Omega_m} \sigma(\nabla V)\cdot(\nabla V')\,\mathrm{d}\Omega_m + \sum_{i\in F} \widetilde{I}_i\widetilde{V}_i(V') = 0, \tag{6}$$

where Ω_m denotes the domain corresponding to the normal-conductive matrix.

2.2.3. Circuit-coupling equations. After traveling a distance ℓ, the periodicity length-defined as the distance along z at which each filament occupies the position of another-each filament takes the place of its adjacent one. Extending this concept to all filaments $i \in N_f$, this yields to:

$$\widetilde{I}_j = I_k - I_i, \tag{7}$$

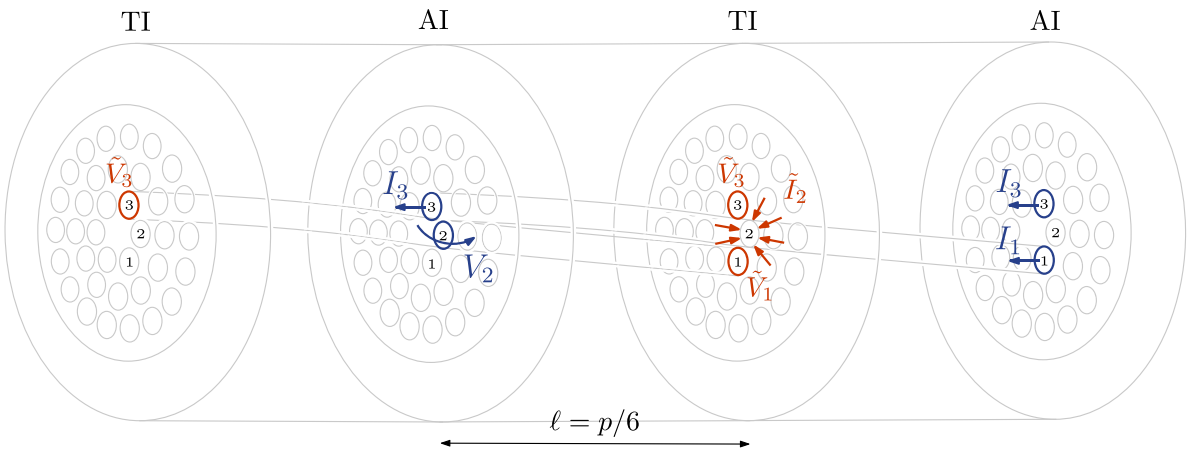

Figure 6. The figure illustrates the coupling between the AI (magnetodynamic) problem and the TI (stationary) problem. This coupling occurs through global variables, which are interconnected based on circuit considerations.

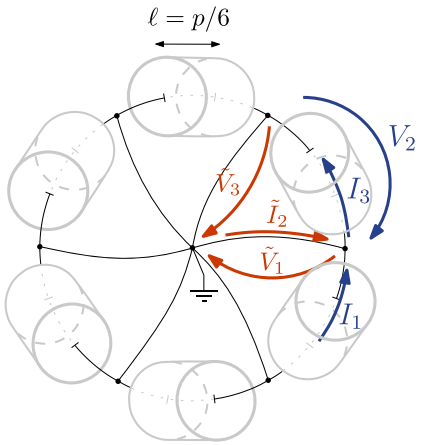

Figure 7. 2D graphical representation illustrating the coupling between the global variables V_2 (AI), $\widetilde{V}_1$ and $\widetilde{V}_3$ (TI) and I_1, I_3 (AI) and $\widetilde{I}_2$ (TI) for the six filaments in the inner layer. The coupling is achieved via the circuit equations (7) and (8), interconnected at a grounded reference node.

$$V_j = \widetilde{V}_k - \widetilde{V}_i. \tag{8}$$

We elucidate the implications of equations (7) and (8) through a straightforward example with $N_\mathrm{f} = 36$ filaments depicted in figure 6. Leveraging the periodicity of the cross-sections, the disparity between currents I_3 and I_1 equals the accrued current $\widetilde{I}_2$ over the length 2ℓ. Similarly, the difference between voltages $\widetilde{V}_3$ and $\widetilde{V}_1$ equals the accumulated voltage V_2 over the length 2ℓ. Figure 7 presents a 2D graphical representation of the coupling between global variables computed through the two sub-models: AI (see section 2.2.1) and TI (see section 2.2.2).

2.3. Hysteresis in ferromagnetic materials

In this section, we introduce a methodology extensively documented in the literature [34–37], aimed at numerically modeling the hysteretic behavior and associated dissipative losses in ferromagnetic materials. We will provide a concise overview of the methodology's origins and its application to our specific problem: analyzing ferromagnetic hysteresis losses in the resistive matrices of multifilamentary wires made of MgB_2.

The method explicitly accounts for the magnetic pinning effect as a dry friction-like force acting on the magnetic polarization. In contrast to the Preisach [38, 39] and Jiles–Atherton [40] models, this vectorial model is founded on thermodynamic first principles from the outset [41]. The model integrates the thermodynamic representation of hysteresis, as suggested in [34, 36, 42]. The formulation of the model refers explicitly to the first and second principles of thermodynamics [35].

Key assumptions underpinning the model include:

(i) Decoupling of ferromagnetic hysteresis losses and eddy current losses is possible, enabling the separation of the two components in the treatment of the problem. We focus solely on hysteresis losses in this section. The eddy-current sub-problem was extensively elaborated upon in section 2.2.

(ii) Representation of the magnetic flux density field (T), $\mathbf{B} = \mu_0(\mathbf{H}+\mathbf{M}) = \mathbf{B}_0 + \mathbf{B}_\mathrm{M}$, where:
- $\mathbf{B}_0 = \mu_0\mathbf{H}$, denotes the linear and reversible magnetic polarization in linear magnetic materials, represented using vacuum permeability μ_0.
- $\mathbf{B}_\mathrm{M}$ is associated with microscopic moments within the magnetic material, allowing for the representation of nonlinear and irreversible behavior (the magnetic domain in figure 1).

(iii) The interpretation of hysteresis losses entails attributing them to the power delivered by a constant amplitude generalized force aligned with the variation in magnetic polarization, akin to the concept of dry friction in mechanics, figure 8(a). This force emerges from the pinning effect, which acts in opposition to the movement of Bloch walls [30].

These assumptions lay the foundation for the subsequent development and analysis of the hysteresis behavior within the proposed model.

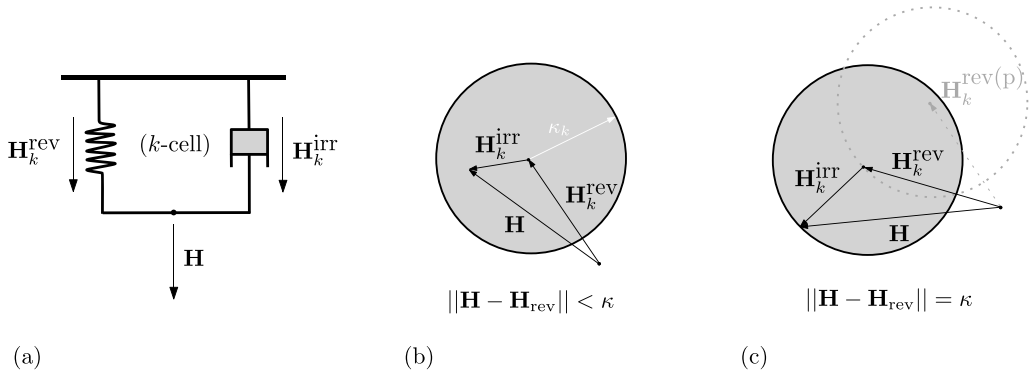

Figure 8. (a) Mechanical analogy and (b), (c) pictorial representation of a single cell within the EB Model.

2.3.1. Ferromagnetic hysteresis modeling. We consider a set of N hysteresis cells, akin to 'play hysterons' [38, 41, 43]. Each cell represents a discrete subsystem, as illustrated in figure 8, and comprises a reversible energy component stored within the magnetic field (rev) and an irreversible component representing dissipative hysteresis losses (irr). For each cell $k \in \{1,\dots,N\}$, the total applied magnetic field is decomposed into reversible and irreversible parts, $\mathbf{H}_k^{\text{rev}}$ (A m^{-1}) and $\mathbf{H}_k^{\text{irr}}$ (A m^{-1}), respectively, as follows

$$\mathbf{H} = \mathbf{H}_k^{\text{rev}} + \mathbf{H}_k^{\text{irr}}. \tag{9}$$

The magnetic flux density $\mathbf{B}$ (T) solely depends on the reversible field. It is expressed as

$$\mathbf{B} = \mu_0 \mathbf{H} + \sum_{k=1}^{N} \omega_k \mathbf{J}_{\text{an}}\left(\mathbf{H}_k^{\text{rev}}\right), \tag{10}$$

where $\mathbf{J}_{\text{an}}$ denotes an anhysteretic function characterizing the material, and the weights ω_k sum up to 1. For ferromagnetic materials, this function typically adheres to a saturation law, introducing a non-linearity to the model [30].

Another source of non-linearity arises from the hysteresis cell update rule outlined below. The irreversible part predominantly governs the hysteresis behavior. The vector play model suggests the following explicit update rule, starting from a known previous solution $\mathbf{H}_k^{\text{rev(p)}}$ of the reversible component of the vector magnetic field

$$\begin{aligned}\mathbf{H}_k^{\text{rev}} &= U_k\left(\mathbf{H}, \mathbf{H}_k^{\text{rev(p)}}\right) \\ &= \begin{cases} \mathbf{H}_k^{\text{rev(p)}} & \text{if } \|\mathbf{H}-\mathbf{H}_k^{\text{rev(p)}}\| \leqslant \kappa_k, \\ \mathbf{H} - \kappa_k \frac{\mathbf{H}-\mathbf{H}_k^{\text{rev(p)}}}{\|\mathbf{H}-\mathbf{H}_k^{\text{rev(p)}}\|} & \text{otherwise,} \end{cases}\end{aligned} \tag{11}$$

where κ_k (A m^{-1}) is a parameter defining the radius of the kth play operator, figures 8(b) and (c). Together with the weights ω_k and the form of $\mathbf{J}_{\text{an}}$, the parameters κ_k fully characterize the hysteresis model.

It is important to note that the vector play model offers a simplified representation of the thermodynamically accurate energy-based model [41]. It accurately applies in scenarios involving unidirectional or purely rotational excitations

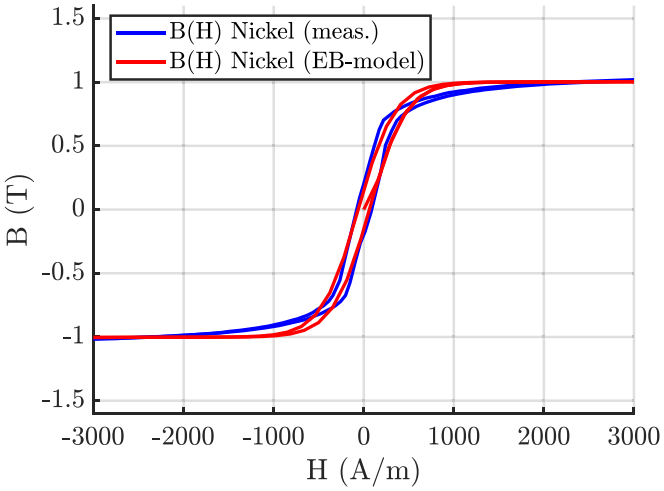

Figure 9. The figure presents the measured magnetization cycle of a cylindrical Nickel wire specimen with a diameter of 0.83 mm and a length of 4 mm, with the applied external magnetic field oriented perpendicular to the sample's axis. The magnetization cycle was recorded at the Institute of Electrical Engineering (IEE) of SAS in Bratislava, Slovakia. Nickel, being a ferromagnetic material, displays soft ferromagnetic properties, as indicated by its low coercive field.

or when $\mathbf{J}_{\text{an}}$ follows a linear law (not applicable to ferromagnetic materials), but remains an approximation in other cases.

The instantaneous power density, denoted as P (W m^{-3}), can be decomposed into stored and dissipated components. Referring to equation (10), the total instantaneous dissipated power can be expressed as

$$\begin{aligned} P &= \mathbf{H}\cdot\dot{\mathbf{B}} \\ &= \mathbf{H}\cdot\left(\mu_0\dot{\mathbf{H}} + \sum_{k=1}^{N}\omega_k \dot{\mathbf{J}}_{\text{an}}\left(\mathbf{H}_k^{\text{rev}}\right)\right) \\ &= \mathbf{H}\cdot\left(\mu_0\dot{\mathbf{H}}\right) + \sum_{k=1}^{N}\omega_k \mathbf{H}_k^{\text{rev}}\cdot\dot{\mathbf{J}}_{\text{an}}\left(\mathbf{H}_k^{\text{rev}}\right) \\ &\quad + \sum_{k=1}^{N}\omega_k \mathbf{H}_k^{\text{irr}}\cdot\dot{\mathbf{J}}_{\text{an}}\left(\mathbf{H}_k^{\text{rev}}\right). \end{aligned} \tag{12}$$

Table 1. Main parameters of the wires under investigation.

WM36/WM36-Cu† design wire, see figure 10(a)	
SC/non-SC ratio	17%
Number of filaments, N_f	36
Wire external radius, R_{ext} (Monel)	0.5 mm
Wire external radius, R_{int} (Nickel)	0.34 mm
Filament radius, R_{fil} (MgB_2)	35 μm
†Copper-plated thickness (only for WM36-Cu)	30 μm
Filament twist pitch length, p	90 mm
Minimal critical current at 20 K	400 A at 1 T
WM6/WM6-Cu† design wire, see figure 10(b)	
SC/non-SC ratio	26%
Number of filaments, N_f	6
Wire external radius, R_{ext} (Monel)	0.765 mm
Wire external radius, R_{ixt} (Nickel)	0.57 mm
Filament radius, R_{fil} (MgB_2)	164 μm
†Copper-plated thickness (only for WM6-Cu)	30 μm
Filament twist pitch length, p	>2000 mm
Minimal critical current at 20 K	865 A at 1.4 T
Copper wire (figure 10(c)), for $\rho(T)$ please refer to figure 11	
Wire radius, R_{ext}	0.685 mm
RRR_{Cu}	230 (−)
Nickel200 wire (figure 10(c)), for $\rho(T)$ please refer to figure 11	
Wire radius, R_{ext}	0.415 mm
RRR_{Ni}	5/7 (−)
Nickel200 tube (figure 10(c)), for $\rho(T)$ please refer to figure 11	
Wire radius, R_{ext}	5.08 mm
Wire radius, R_{int}	2.28 mm
RRR_{Ni}	5/7 (−)

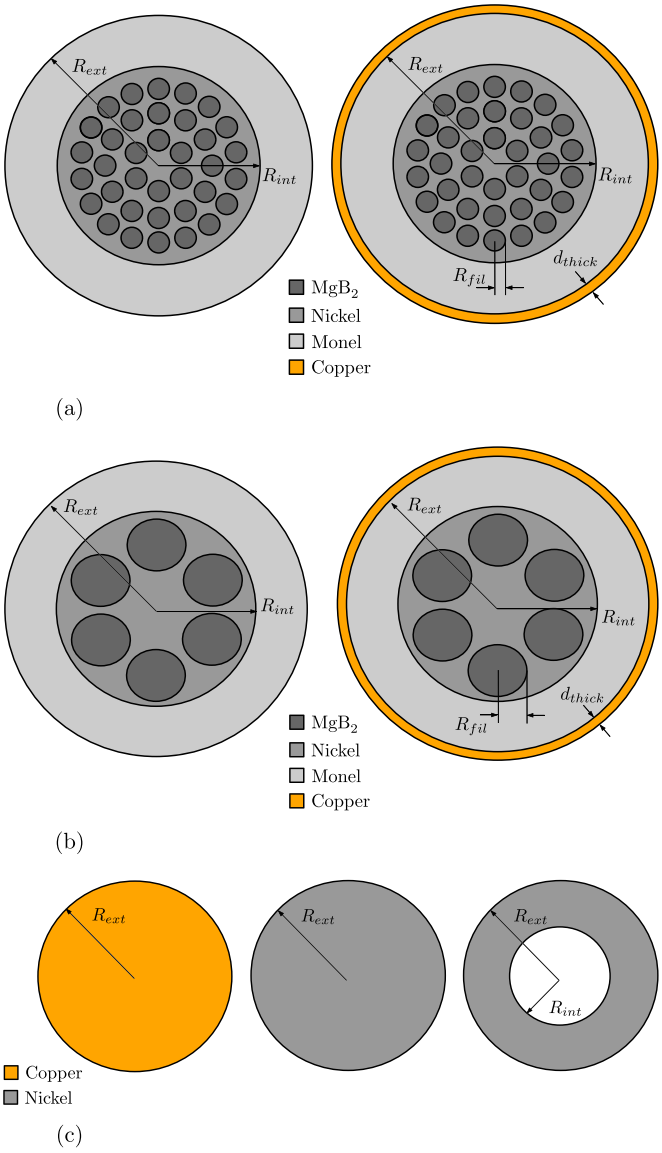

Figure 10. (a)-Left WM36 and (a)-Right WM36-Cu design wires. (b)-Left WM6 and ((b)-Right) WM6-Cu design wires. (c)-Left Copper, (c)-center Nickel wires and (c)-right Nickel tube used for comparison with WM36/WM36-Cu and WM6/WM6-Cu. Detailed information in table 1.

From equation (12), two distinct contributions can be identified:

$$P^{\text{rev}} = \mathbf{H}\cdot\left(\mu_0\dot{\mathbf{H}}\right) + \sum_{k=1}^{N}\omega_k\mathbf{H}_k^{\text{rev}}\cdot\dot{\mathbf{J}}_{\text{an}}\left(\mathbf{H}_k^{\text{rev}}\right), \tag{13}$$

$$P^{\text{irr}} = \sum_{k=1}^{N}\omega_k\mathbf{H}_k^{\text{irr}}\cdot\dot{\mathbf{J}}_{\text{an}}\left(\mathbf{H}_k^{\text{rev}}\right) = \sum_{k=1}^{N}\omega_k\left(\mathbf{H}-\mathbf{H}_k^{\text{rev}}\right)\cdot\dot{\mathbf{J}}_{\text{an}}\left(\mathbf{H}_k^{\text{rev}}\right). \tag{14}$$

With equation (14), the instantaneous hysteretic ferromagnetic contribution to losses for the wire can be computed.

3. Wire design under investigation

In this section, we detail the wire designs investigated in this study, all of which are marketed by ASG Superconductors. Their principal parameters are summarized in table 1.

Figures 10(a)–(c) illustrate the sample designs used in both the numerical and experimental studies.

The wire designs examined include the 36-filament WM36 design and the 6-filament WM6 design. For each of these two designs, an alternative version was also considered, featuring a copper-plated metallic sheath deposited on the outside of the wires. Additionally, we include two purely metallic wires and a metallic tube, made of copper ($RRR_{Cu} = 230$) and Nickel (Ni200, $RRR_{Ni} = 5$), used in both numerical and experimental studies to compare the losses with those of purely metallic wires, detailed in figure 10(c). The properties of copper and Nickel used in the simulations were measured on pure material samples that underwent thermal and mechanical processes analogous to those present in the tests. Resistivity

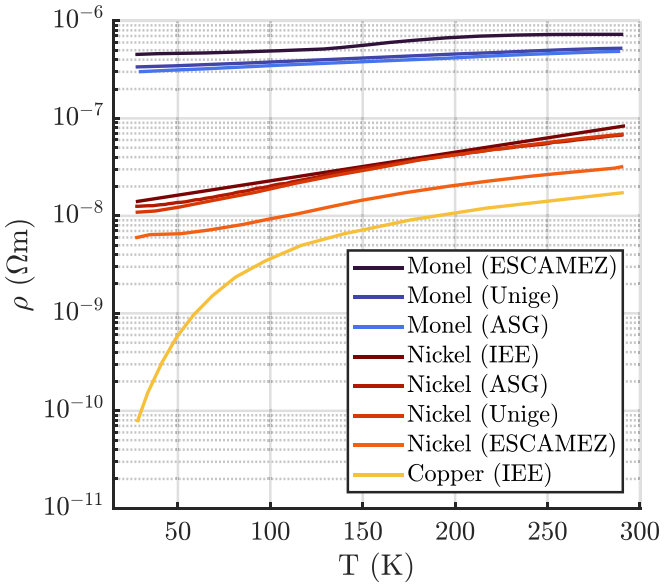

Figure 11. Experimental measurements conducted on selected Nickel and Monel wires. These measurements do not pertain to the exact same wire or material sample; they were conducted non-simultaneously and in different laboratories, employing varied techniques and instrumentation. Precise comparison of experimental values extends beyond the scope of this study. The aim is solely to illustrate what might constitute an acceptable value at the numerical modeling level for some of the most relevant properties of the stabilizing material used in MgB_2 wires. Measurements denoted by 'ESCAMEZ' were obtained from [44]. The resistivity values used in this study are those provided by the IEE-SAS Institute in Bratislava, denoted as 'IEE' in the legend.

measurements were performed through four-probe measurements. The same measurements were conducted across multiple laboratories at University of Genoa , Institute of Electrical Engineering SAS , and ASG Superconductors S.p.a. (respectively Unige, IEE and ASG in figure 11). The results were successfully compared with findings from the literature on similar material samples obtained from [44] (ESCAMEZ in figure 11). Although the samples were not identical, the comparison of similar samples can provide valuable insights when selecting parameters for numerical simulations. Notably in all the simulations performed in this study, the parameters used were those one obtained with the IEE-SAS measurements.

In addressing the magnetic sub-problem, the parameters of ferromagnetic materials are systematically and accurately identified using standard DC or quasi-static measurement techniques applied to Nickel and Monel samples. To reproduce the ferromagnetic behavior of these materials, and in reference to the numerical model previously introduced in section 2.3, $N = 3$ cells are utilized, resulting in a total of six parameters: $\kappa_1 = 0$, $\kappa_2 = 500$, $\kappa_3 = 1200$, and $\omega_1 = 0.1$, $\omega_2 = 0.65$, $\omega_3 = 0.25$. These parameters were determined through iterative adjustments to ensure that the $B(H)$ loop obtained from the numerical model closely matches the experimental measurements.This enables the generation of the red curve depicted in figure 9, which is designated as the *EB-model*. This model is subsequently compared with the measured curve, represented in figure 9 by the blue curve.

4. Comparison of numerically computed and measured losses

This section delves into the process of deriving numerical results used for comparing with experimental results. We highlight the methodology used for addressing the eddy-current sub-problem within the numerical model, as elaborated in [32], as previously outlined in section 2.2, with the incorporation of a non-linear permeability for magnetic materials. Conversely, for the ferromagnetic sub-problem, which deals with hysteresic ferromagnetic losses, we will refer to the methodology already introduced in section 2.3.

4.1. Dissipative losses for pure Copper and Nickel wires

The validation process unfolds alongside an analysis of dissipative behavior, initially focusing on purely metallic wires. This approach gradually complicates the analyzed physical problem, building upon the principal dissipative mechanisms outlined in section 1. The initial case study involves analyzing dissipative processes in a wire composed solely of copper, representing the simplest scenario. As delineated in the mechanisms described in the preceding sections, dissipative effects arising from parasitic currents primarily account for wire losses (the (i) contribution represented in figure 1). Hence, the analysis employed a simplified 2D model, model whose results replicate the behavior of an infinitely long constant-section wire, without accounting for edge effects or current closure at wire ends. The external source field comprised a sinusoidal, spatially uniform and perpendicular magnetic field at varying frequencies, with peak B field values set to 18 mT and 100 mT. The numerical and experimental results are represented in figure 12(a), and exhibit a remarkable agreement.

Subsequently, a similar analysis was performed on a wire composed entirely of nickel, introducing additional dissipative processes beyond those associated solely to eddy currents. The inclusion of magnetic materials complicates the problem due to the inherently nonlinear nature of nickel's magnetic permeability, requiring iterative algorithms to solve the nonlinear system of equations. Unfortunately, literature offering guidance on the most suitable modeling approach in this context is limited, with insights primarily derived from [20] and [45]. Indeed, this study aims to evaluate the requirement for faithfully reproducing the magnetic behavior of the material. The precise comparison between computed losses and experimental data obtained from a wire exclusively made of nickel serves as a model calibration step, intending to accurately replicate the material's magnetic behavior. This comprehensive approach allows a better understanding of incorporating each material's characteristics, as aggregating all factors indiscriminately would obscure their relative contributions to the total losses in the multifilamentary MgB_2 wire. Additional dissipative phenomena due to the ferromagnetic properties of

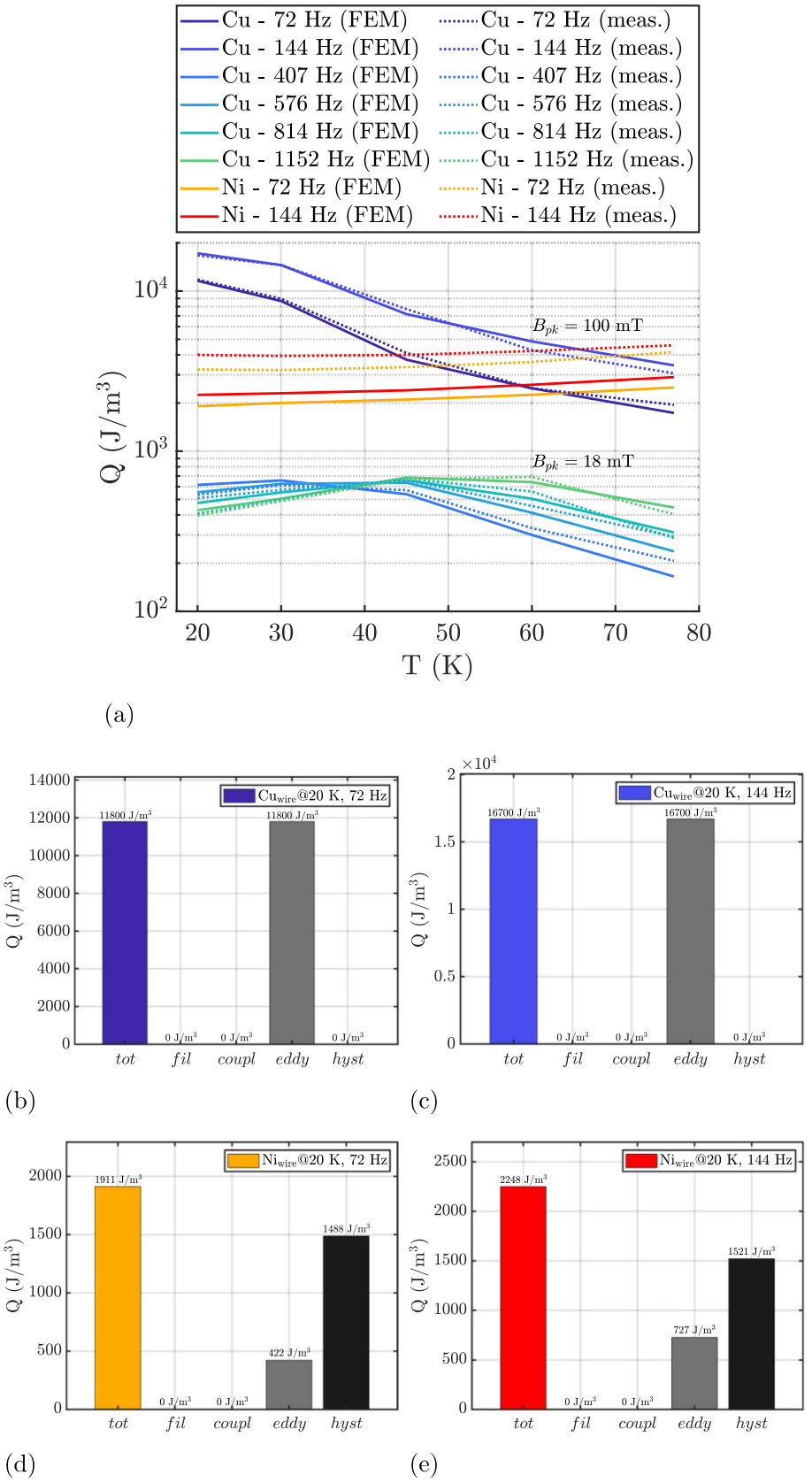

Figure 12. Graphs (a) compare computed losses per cycle (J m^{-3}) with experimental measurements on the copper and nickel samples at varying temperatures and frequencies. The plots in shades of purple and red correspond to applied peak fields of 100 mT, while those in blue/green correspond to a peak field of 18 mT. Subfigures (d) and (e) show nickel tube losses at 72 Hz and 144 Hz, with observable ferromagnetic hysteresis contributions. In the histograms, the label *'fil'* indicates losses in the superconductor, while *'coupl'* refers to coupling losses, which are not present in these normal material samples.

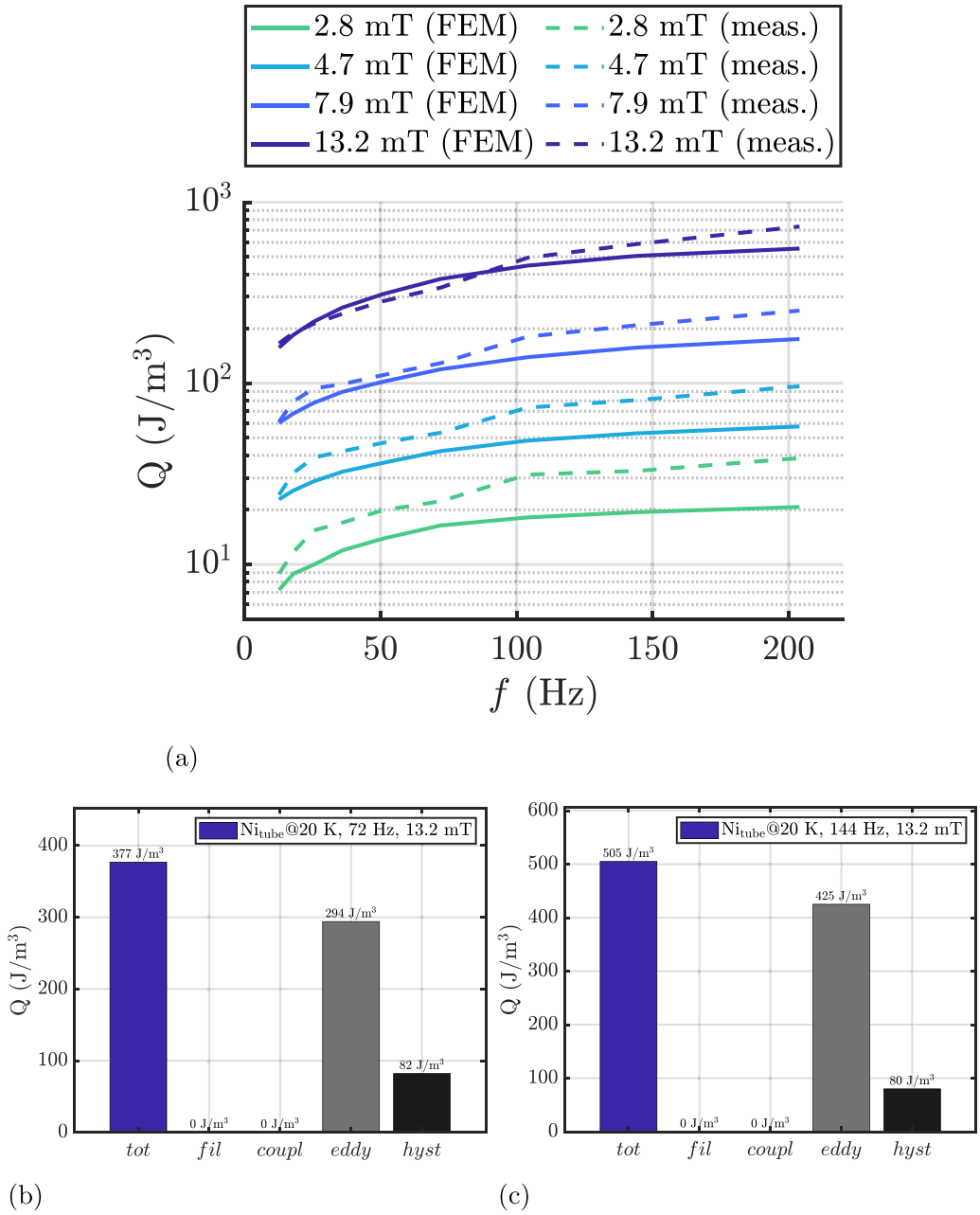

Figure 13. Graphs (a) compare computed losses per cycle ($\mathrm{J\,m^{-3}}$) with experimental measurements on the Nickel tube at varying frequencies and peak magnetic field. Subfigures (b) and (c) illustrate the nickel tube losses at 72 Hz and 144 Hz, highlighting observable ferromagnetic hysteresis contributions.

Nickel, compared to a metallic wire exhibiting diamagnetic or paramagnetic behavior, can be summarized into two primary contributions:

(i) The first effect stems from the intrinsic characteristic of the saturation curve of a ferromagnetic material. It is well-established that the magnetic permeability of such materials depends on the applied magnetic field, $\mathbf{H}$ ($\mathrm{A\,m^{-1}}$). However, the intriguing aspect lies in the implications of this characteristic under sinusoidally varying magnetic fields over time, and the resulting combined effects on induced losses due to parasitic currents. This effect is depicted in figure 14, illustrating how the nonlinear characteristic of the material's permeability increases induced currents when the $\mathbf{H}$ field component in the direction of the applied field crosses zero. This phenomenon occurs as we venture into a region of material operation where the magnetic permeability significantly surpasses that of air (μ_0). In other words, under similar operating conditions, if the permeability is tens of times greater than that of air ($\mu = \mu_r\mu_0 >> \mu_0$), according to Faraday–Neumann's law, the induced electromotive force (emf) in the material will be higher. Given the material's conductivity, this escalation in emf results in increased currents and, consequently, increased losses. Notably, this effect finds a

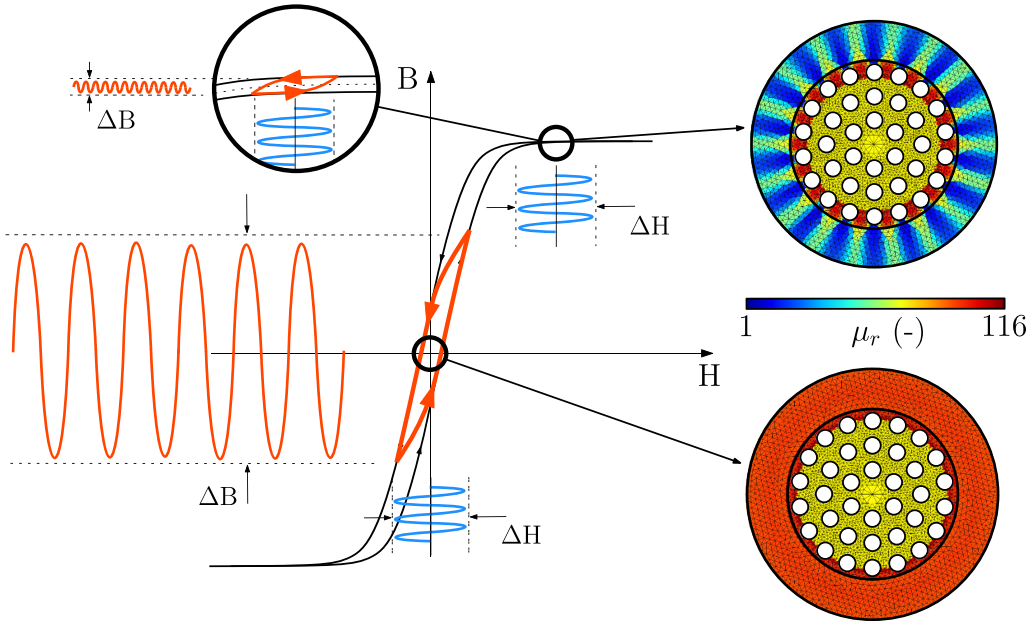

Figure 14. Demonstration of how the induced currents in a magnetic material vary based on its magnetic behavior as represented by its magnetization curve. Depending on whether the material is in a state of saturation-with a differential permeability similar to that of air-or not, the induced currents will differ. In the saturation state, for the same external variation of the **H** field, there will be a smaller change in the magnetic field **B** over the same period of time. Consequently, the induced electromotive forces (emfs) will be lower, leading to reduced eddy currents and thus lower Joule losses, situation in the upper subfigure. Conversely, in the situation of the lower subfigure, for a purely sinusoidal field passing through zero, the material is in a state of high permeability. As a result, the induced emfs and parasitic currents will be high, leading to increased dissipative losses.

comprehensive explanation within an eddy-current model, obviating the need for resorting to ferro-hysteresis models.

(ii) Any fluctuation in magnetic flux density within a magnetic material inevitably leads to energy dissipation within the material, primarily in the form of irretrievable energy, dissipated as heat. This phenomenon is commonly referred to as *ferromagnetic* hysteresis losses (or *iron* losses). The area enclosed by a closed hysteresis loop during a magnetization cycle carries significant physical significance, representing the precise amount of energy per unit volume irreversibly transformed into heat, given by

$$Q = \oint \mathbf{H} \cdot \mathrm{d}\mathbf{B} \quad \left(\mathrm{J\,m^{-3}}\right), \tag{15}$$

where the integral is performed over a cycle of the external varying magnetic source. Figure 9 presents a typical hysteretic loop for a soft ferromagnetic material, illustrating this concept. The power loss density, P, related to equation (15), is deduced by expressing the dissipation per unit time instead of unit cycle, thus

$$P = f \oint \mathbf{H} \cdot \mathrm{d}\mathbf{B} \quad \left(\mathrm{W\,m^{-3}}\right), \tag{16}$$

where f (Hz) is the frequency of the external varying magnetic field.

The computed losses for this case study, considering a wire entirely made of nickel, are depicted in figure 12(a), with the different distinct contributions highlighted in figures 12(d) and (e). A discrepancy of approximately 50% is observed for nickel at 72 Hz and 144 Hz, for which no definitive explanation has been identified. This difference may arise from experimental uncertainties, material inhomogeneities, or limitations in the modeling assumptions. Further investigation would be required to clarify its origin. A concise overview of the model employed for calculating magnetic hysteresis losses is provided in section 2.3.

Tests were subsequently performed using a different sample for the measurements. The nickel wire was replaced with a tube, which was subjected to the same type of external magnetic field as before, but at a fixed temperature of 20 K. The frequency range spanned from 12 Hz to 204 Hz, and the peak magnetic field varied from a minimum of 2.8 mT to a maximum of 13.2 mT. The results are shown in figure 13, and are compared with numerical FE results obtained using the previously described numerical model. It is worth noting that the discrepancy between simulations and measurements becomes more pronounced at very low peak fields (a few to tens of millitesla), suggesting possible field-dependent effects or measurement uncertainties. However, this is observed only in calibration data, while at higher fields (hundreds of millitesla), the agreement remains excellent. Figure 15 illustrates the magnetic field and current density numerically computed for the designs analyzed in this initial phase of the study.

This energy-based hysteresis model is rate-independent, serving as a simplification of reality. Once these material parameters are identified, they comprehensively define the material in a localized manner, enabling quantitative predictions of losses across various frequencies.

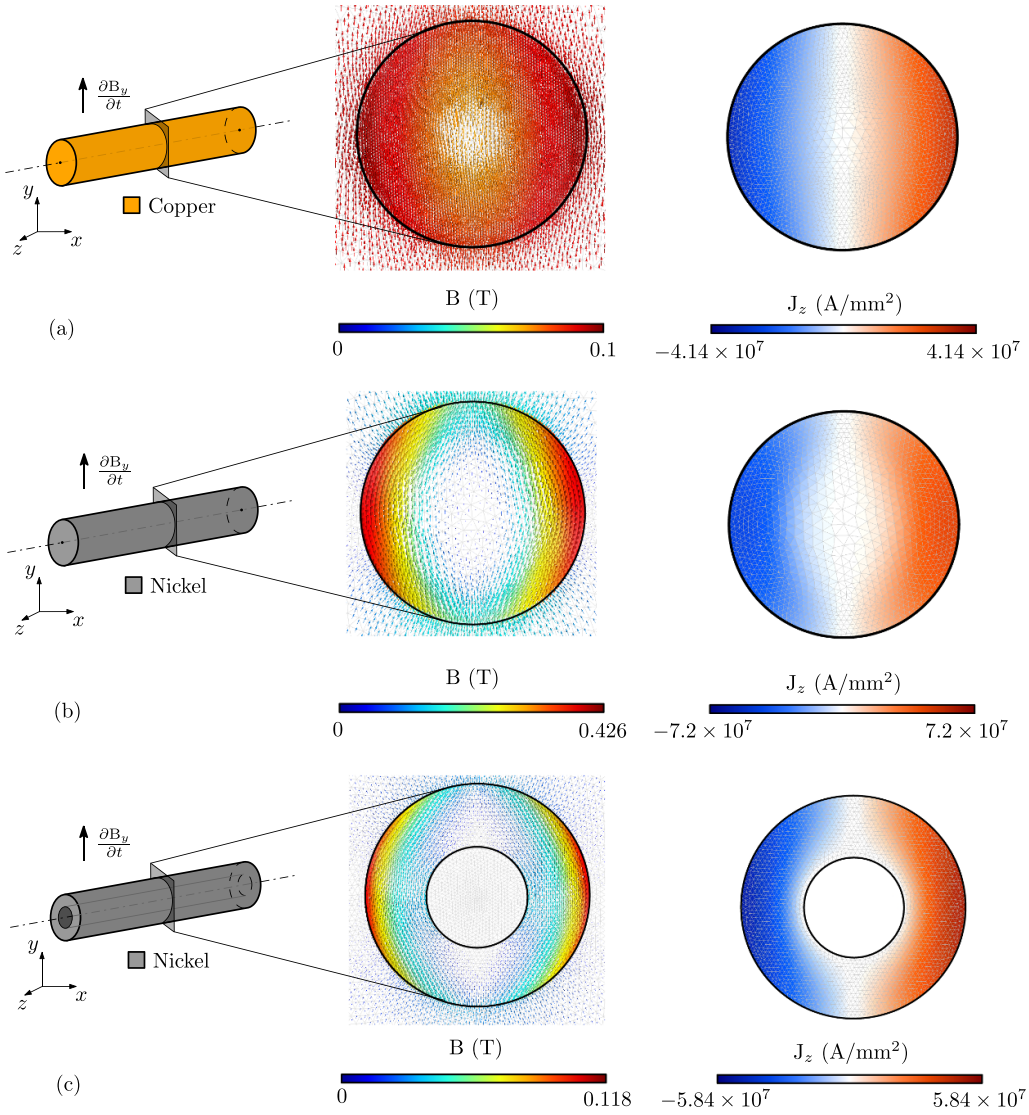

Figure 15. Computed magnetic field and current density at 72 Hz are shown for the three resistive designs used in the first part of the study: (a) copper wire, (b) nickel wire, and (c) nickel tube.

4.2. Dissipative losses for WM36 and WM6 Wire

In this section, we discuss dissipative losses for the WM36 and WM6 design wires, specifically the multifilamentary MgB_2 wires used as a case study.

In this case study the ferromagnetic hysteresis component of dissipative loss originates from the magnetic properties of the materials employed as stabilizers. Given the complexity of these multifilamentary wires and all the different properties of the materials involved, discerning the contribution of each component to the total losses is challenging.

The measured and numerically computed losses are presented in figures 17 and 19, from which several valuable insights can be gleaned. It is evident that the losses exhibit minimal frequency dependence, particularly for the WM36/WM6 designs (without copper). Doubling the frequency results in increased losses, but only by a limited percentage, indicating that the total losses are not strongly frequency-dependent. The total losses do not appear to include a significant component attributed to coupling or eddy current losses in J m^{-3} (per cycle). Consequently, a predominant 'rate-independent' component, independent of the frequency of the external magnetic field signal, is observed.

As discussed in the previous section and given the observed rate-independent contribution, the identified losses are predominantly characterized by hysteresis behavior. Specifically, these losses are attributed to ferromagnetic losses (component (iv) in figure 1) and losses due to magnetization in the SC material (component (ii) in figure 1). Notably, even after the wire's transition temperature (T_c) of approximately 37 K, the hysteresis-like behavior of the losses persists. This persistence indicates a significant dissipative component attributed to ferromagnetic losses in materials such as nickel and monel within the wire matrix. Figures 17(b), (c) and 19(b), (c) show the different contributions calculated numerically for the WM36/WM6 designs at frequencies of 72 Hz and 144 Hz,

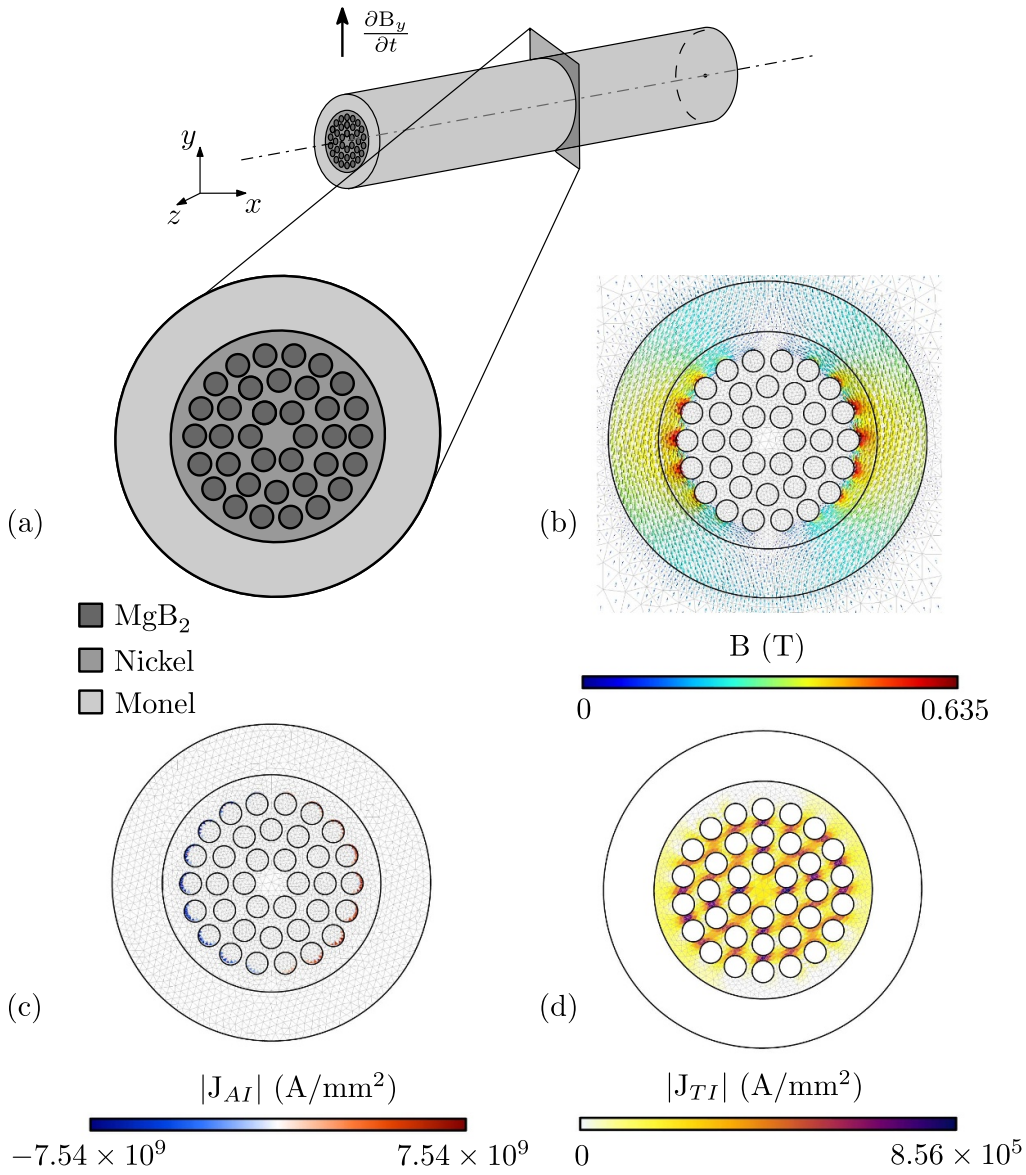

Figure 16. Displayed for the WM36 design (a) are the computed magnetic field (b), and the computed current density for the two subcases described in section 2.2: the out-of-plane subproblem current density $|J_{\mathrm{AI}}|$ in (c) and the in-plane subproblem current density $|J_{\mathrm{TI}}|$ in (d).

respectively. It is evident that the hysteresis losses in ferromagnetic materials contributes substantially to the total losses.

Referring to figures 17 and 19, it is interesting to note that the losses for the WM36 and WM6 designs remain almost constant up to a temperature of 33 K. This is due to the nearly constant electrical resistivity ρ (Ωm) of monel and nickel as a function of temperature in this 20–33 K range, see figure 11. Above 33 K, the losses increase due to the decrease in the wire's critical current, which allows greater penetration of screening currents. The losses peak at the wire's critical temperature (37 K) and then decrease, settling at a value that corresponds almost entirely to the contribution of ferromagnetic losses from the stabilizing materials.

The same considerations can be made for the WM36-Cu and WM6-Cu designs. The primary difference observed is the greater dependence of losses in these designs on temperature changes. This is due to the fact that in these designs, where a copper-plated sheath is present, the losses are predominantly attributed to the copper itself, see figures 17(d), (e) and 19(d), (e). Given the higher sensitivity of copper resistivity to temperature variations, this results in an initial reduction of losses as the temperature increases. This occurs because the resistivity of copper is rising, as illustrated in figure 11, leading to a decrease in the induced parasitic currents within the wire sample. Figures 16 and 18 present physical quantities computed using the developed numerical tool, including the magnetic field and current density.

The results clearly show that, despite the significant differences between the WM36 and WM6 wires, the twist pitch has a limited impact on loss reduction. Specifically, when using a twist pitch of 90 mm or greater than 2000 mm and assuming the same resistivity for the Nickel matrix, the filaments remain coupled in both cases. This behavior resembles that of a monofilament, where current penetration occurs only

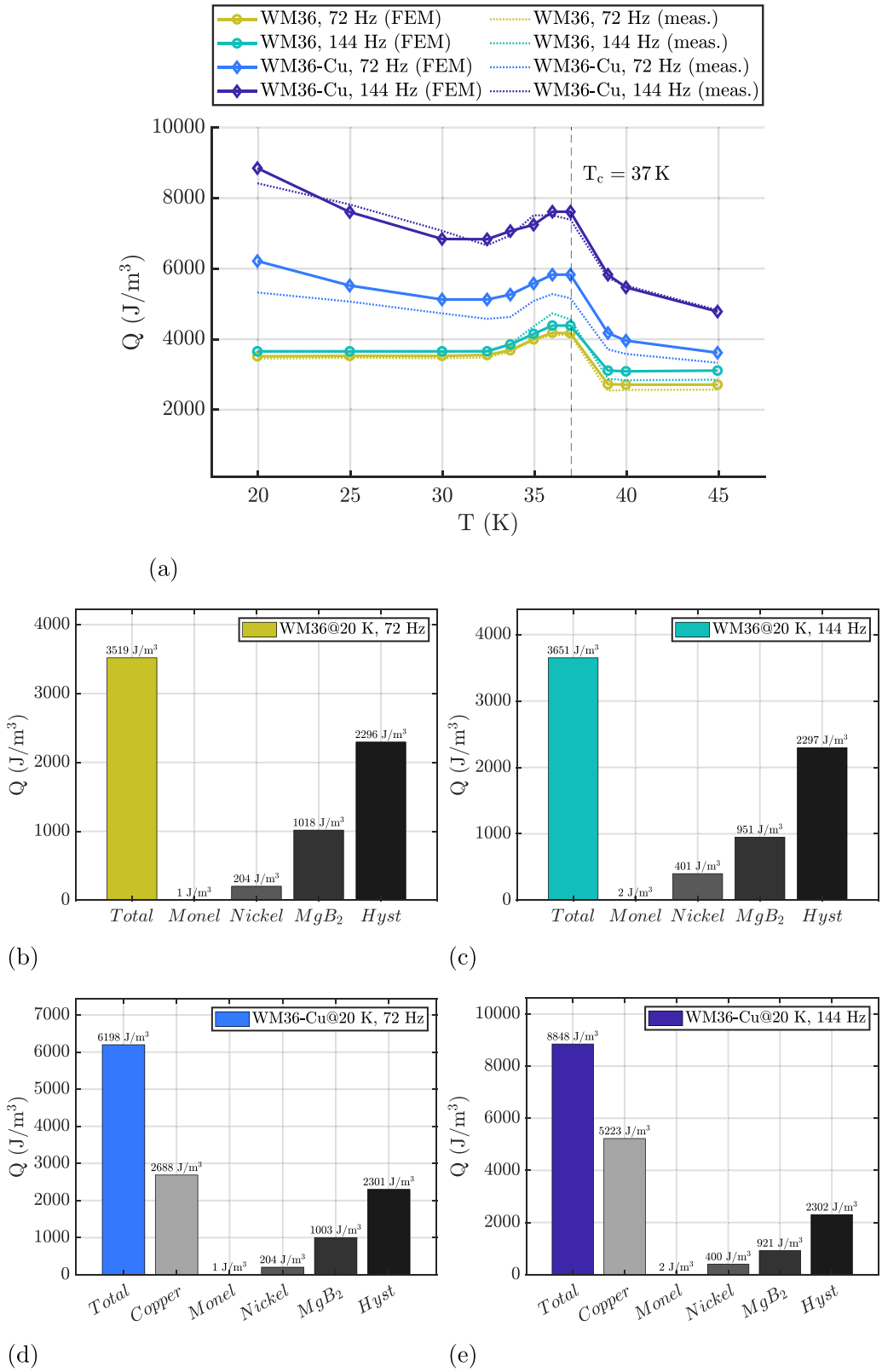

Figure 17. Graphs (a) compare computed losses per cycle (J m^{-3}) with experimental measurements on the WM36 wire at varying temperatures and frequencies. Subfigures (b) and (c) illustrate the WM36 losses at 72 Hz and 144 Hz, while subfigures (d) and (e) show the WM36-Cu losses at the same frequencies. In the histograms, the 'MgB_2' contribution represents only superconducting hysteresis losses, while *'Hyst'* losses refer to ferromagnetic hysteresis losses in Nickel and Monel. The approach used in this study was to sum the relative contributions of eddy losses and coupling losses in *'Nickel'* and *'Monel'*, respectively. The temperature for the measurements shown in the histograms is 20 K, and the applied peak field is 0.1 T.

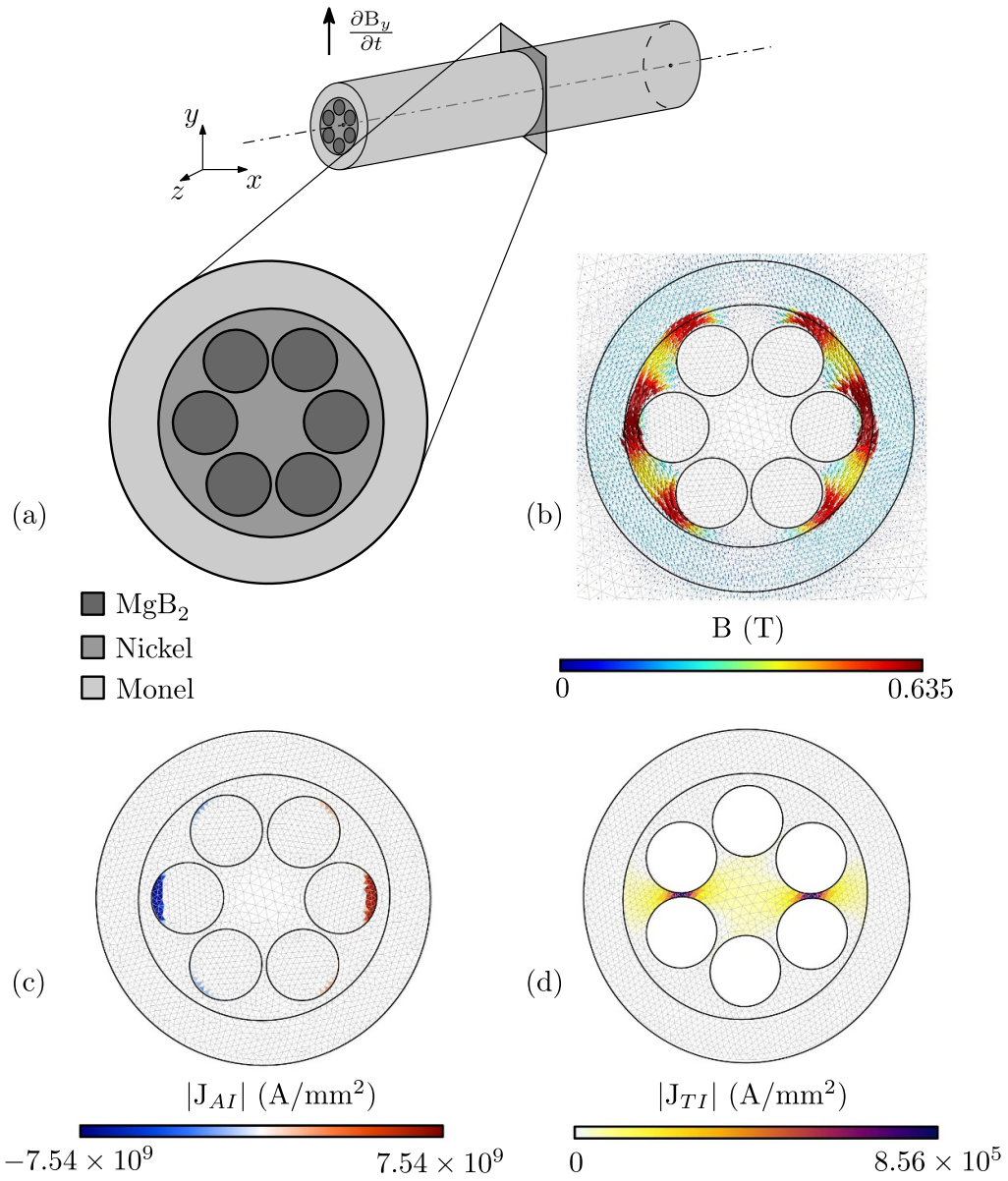

Figure 18. Displayed for the WM6 design (a) are the computed magnetic field (b), and the computed current density for the two subcases described in section 2.2: the out-of-plane subproblem current density $|J_{\mathrm{AI}}|$ in (c) and the in-plane subproblem current density $|J_{\mathrm{TI}}|$ in (d).

in the filaments belonging to the outermost layer, while the inner layer filaments remain completely shielded. Within the examined frequency range (72–144 Hz), all filaments within the bundle are fully coupled. As a result, the associated SC-hysteretic losses are substantial, comparable to those of a monofilament with the same overall dimensions as the wire. However, this behavior may change at different frequencies. At the examined frequencies, the coupling currents are not significantly affected by the skin effect and therefore distribute rather uniformly across the entire matrix cross-section, as shown in figures 16(d) and 18(d). Another important aspect to consider is that the peak magnetic field used in the experiments was limited by measurement system constraints, reaching only 0.1 T. In contrast, the penetration field for this wire (in the absence of transport current) exceeds 5 T. It is therefore reasonable to expect different results when considering higher magnetic fields or the presence of transport current. Under such conditions, modifying the twist pitch of the filaments could potentially have a more pronounced effect on the observed behavior.

The proposed method, rooted in 2D modeling, provides a significant reduction in computational expense compared to traditional 3D methodologies. For the examined scenarios, computation times were reduced to under an hour on a standard workstation featuring an Intel® Core™ i9-9960X CPU @3.10 GHz and 256 GB of RAM. This substantial improvement in efficiency facilitates the execution of extensive parametric studies and detailed analyses of strand behavior across diverse configurations. These advancements enable comprehensive exploration and optimization of design parameters

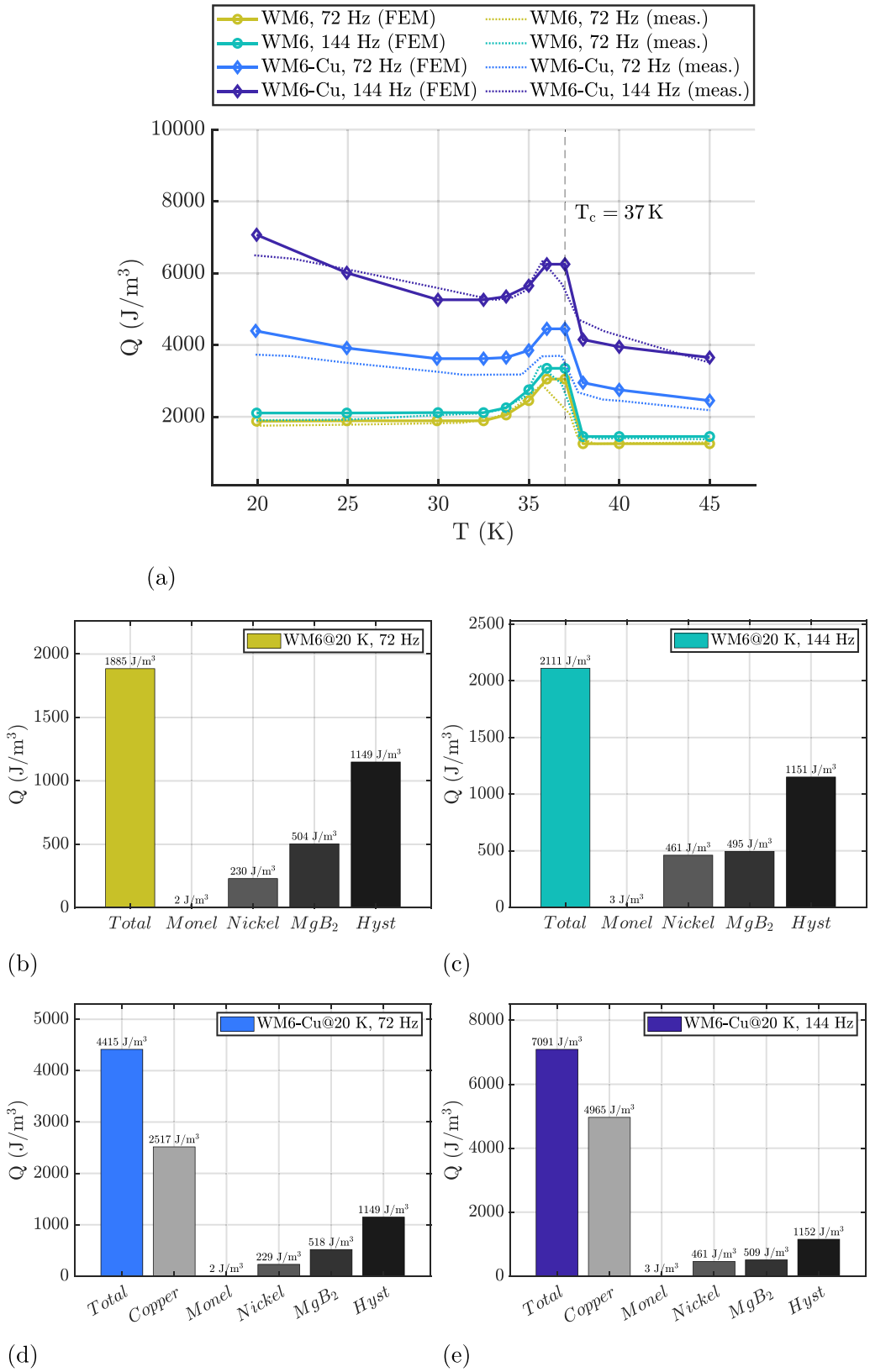

Figure 19. Graphs (a) compare computed losses per cycle (J m^{-3}) with experimental measurements on the WM6 wire at varying temperatures and frequencies. Subfigures (b), (c) illustrate the WM6 losses at 72 Hz and 144 Hz, while subfigures (d), (e) show the WM6-Cu losses at the same frequencies. In the histograms, the 'MgB_2' contribution represents only superconducting hysteresis losses, while *'Hyst'* losses refer to ferromagnetic hysteresis losses in Nickel and Monel. The approach used in this study was to sum the relative contributions of eddy losses and coupling losses in *'Nickel'* and *'Monel'*, respectively. The temperature for the measurements shown in the histograms is 20 K, and the applied peak field is 0.1 T.

within practical timeframes and with moderate computational resources, supporting both detailed investigations and iterative design processes.

5. Conclusion

In this study, we have developed an advanced numerical model to accurately calculate losses in SC multifilamentary wires that incorporate ferromagnetic stabilizing materials. This model, which is open-source, represents the first comprehensive, monolithic approach capable of analyzing all significant loss contributions in MgB_2 wires. A notable feature of this model is its capability to compute both hysteresis losses in ferromagnetic materials and the conventional Joule losses typically assessed in eddy current models, including SC hysteresis losses.

Our findings indicate that the primary contributions to total losses within the wire arise from both hysteresis effects-SC and ferromagnetic, in the considered frequency range. Observations reveal that eddy currents in the resistive matrices contribute minimally to total losses; for example, in Monel, such currents and associated losses remain low due to the material's relatively high resistivity, around 3×10^{-7} Ωm. However, the dominant loss contributions associated with Nickel and Monel primarily stem from their ferromagnetic behavior. Furthermore, when an external copper sheath is present, it largely dominates the loss profile due to the high eddy current losses induced at relevant frequencies. This occurs as the resistivity of copper at cryogenic temperatures is several orders of magnitude lower than that of Nickel and Monel, at approximately 1×10^{-10} Ωm.

Our analysis also reveals that the wire behaves effectively as a single large filament due to the coupling between individual filaments, which is influenced by the operating frequencies and matrix materials. In this context, altering the twist pitch of the matrix does not significantly affect the losses, as shown by the two designs analyzed, which feature a large variation in twist pitch but show no substantial reduction in losses. Our measurements confirm that at the applied range of frequencies and with the given matrix materials, the filaments remain fully coupled. As a result, reducing the filament size alone does not effectively lower SC hysteresis losses, since these losses scale with the overall cross-sectional area of the coupled structure rather than the size of individual filaments. For wires of this design, the dominant losses are essentially those of a large monofilament with an equivalent cross-section to the entire filament bundle. Consequently, reducing the total wire cross-section would lead to a decrease in the total wire magnetic moment and a corresponding reduction in hysteresis losses.

A practical guideline for reducing losses in this type of wire involves first verifying, at the operational frequency, whether the filaments are coupled based on the available twist pitch and the resistivity of the matrix. If the filaments are decoupled, it is possible to reduce losses by adjusting the filament size, twist pitch, and the resistivity of the matrix. However, if the filaments are fully coupled, modifying the twist pitch may not decouple them, as this depends on the specific frequency regime to which the wire is subjected. In such cases, one approach to reduce losses is to decrease the total cross-sectional area of the wire, thereby reducing its magnetic moment under the influence of the external field. Naturally, in applications that require a minimum transport current, using multiple wires in parallel may become necessary. Furthermore, altering the ferromagnetic matrix material could lead to improved loss performance, particularly by eliminating the dissipative component linked to ferromagnetic hysteresis losses.

The model's accuracy and reliability have been validated through extensive experimental testing, confirming its ability to provide real-time insights into energy loss mechanisms. Results from the study demonstrate a marked improvement in the accuracy of loss calculations, thereby enhancing our understanding of loss processes in SC multi-filamentary wires. This model establishes a new standard for future research and the design of more efficient SC wires, with significant practical implications for industries focused on optimizing energy efficiency.

Data availability statement

The data cannot be made publicly available upon publication because no suitable repository exists for hosting data in this field of study. The data that support the findings of this study are available upon reasonable request from the authors.

ORCID iDs

L Soldati https://orcid.org/0000-0002-8171-363X
J Dular https://orcid.org/0000-0003-0503-7526
J Kovac https://orcid.org/0000-0001-9127-9681
P Kovac https://orcid.org/0000-0003-1872-0359
M Putti https://orcid.org/0000-0002-4529-1708
M Breschi https://orcid.org/0000-0001-9025-2487

References

[1] Grilli F, Pardo E, Stenvall A, Nguyen D N, Yuan W and Gömöry F 2013 *IEEE Trans. Appl. Supercond.* **24** 78–110
[2] Grilli F 2016 *IEEE Trans. Appl. Supercond.* **26** 1–8
[3] Campbell A 2011 *J. Supercond. Novel Magn.* **24** 27–33
[4] Bossavit A 2000 *Physica B* **275** 142–9
[5] Rhyner J 1993 *Physica C* **212** 292–300
[6] Dular J, Geuzaine C and Vanderheyden B 2019 *IEEE Trans. Appl. Supercond.* **30** 1–13
[7] Lahtinen V and Stenvall A 2014 *J. Supercond. Novel Magn.* **27** 641–50
[8] Stenvall A and Lahtinen V 2019 *IEEE Trans. Appl. Supercond.* **29** 1–7
[9] Stenvall A, Siahrang M, Grilli F and Sirois F 2013 *Supercond. Sci. Technol.* **26** 045011
[10] Lahtinen V and Stenvall A 2012 *IEEE Trans. Appl. Supercond.* **23** 4900505
[11] Bíró O 1999 *Comput. Methods Appl. Mech. Eng.* **169** 391–405
[12] Bossavit A 1985 *COMPEL - Int. J. Comput. Math. Electr. Electron. Eng.* **4** 103–16

[13] Bossavit A 1981 *Comput. Methods Appl. Mech. Eng.* **27** 303–18
[14] Sirois F and Grilli F 2015 *Supercond. Sci. Technol.* **28** 043002
[15] Dular J 2023 Standard and Mixed Finite Element Formulations for Systems with Type-II Superconductors *PhD Thesis* Université de Liège
[16] Raumonen P, Suuriniemi S, Tarhasaari T and Kettunen L 2008 *IEEE Trans. Magn.* **44** 1146–9
[17] Dular J, Henrotte F, Nicolet A, Wozniak M, Vanderheyden B and Geuzaine C 2024 *IEEE Trans. Appl. Supercond.* **34** 1–15
[18] Nicolet A, Zolla F, Agha Y O and Guenneau S 2008 *COMPEL - Int. J. Comput. Math. Electr. Electron. Eng.* **27** 806–19
[19] Soldati L, Dular J, Spina T, Bruzek C E and Breschi M 2025 *IEEE Trans. Appl. Supercond.* **35** 1–5
[20] Escamez G 2016 AC losses in superconductors: a multi-scale approach for the design of high current cables *PhD Thesis* Université Grenoble Alpes
[21] Lyly M, Stenvall A and Mikkonen R 2011 *IEEE Trans. Appl. Supercond.* **22** 4705505
[22] Soldati L, Breschi M, Ribani P L, Spina T and Bruzek C 2024 *IEEE Trans. Appl. Supercond.* **34** 1–5
[23] Riva N, Halbach A, Lyly M, Messe C, Ruuskanen J and Lahtinen V 2023 *IEEE Trans. Appl. Supercond.* **33** 1–5
[24] Nagamatsu J, Nakagawa N, Muranaka T, Zenitani Y and Akimitsu J 2001 *Nature* **410** 63–64
[25] Grasso G, Malagoli A, Ferdeghini C, Roncallo S, Braccini V, Siri A S and Cimberle M R 2001 *Appl. Phys. Lett.* **79** 230–2
[26] Braccini V, Nardelli D, Penco R and Grasso G 2007 *Physica C* **456** 209–17
[27] Malagoli A and Braccini V 2016 Mgb2 wires fabricated using the ex Situ Technique *MgB_2 Superconducting Wires: Basics and Applications* (World Scientific) pp 239–70
[28] Dular P and Geuzaine C 1997 Getdp: a general environment for the treatment of discrete problems
[29] Geuzaine C and Remacle J F 2009 *Int. J. Numer. Methods Eng.* **79** 1309–31
[30] Bertotti G 1998 *Hysteresis in Magnetism: for Physicists, Materials Scientists and Engineers* (Gulf Professional Publishing)
[31] Steinmetz C P 1984 *Proc. IEEE* **72** 197–221
[32] Dular J, Magnus F, Schnaubelt E, Verweij A and Wozniak M 2024 *Supercond. Sci. Technol.* **37** 095002
[33] Jackson J D 2021 *Classical Electrodynamics* (Wiley)
[34] Henrotte F and Hameyer K 2006 *IEEE Trans. Magn.* **42** 899–902
[35] François-Lavet V, Henrotte F, Stainier L, Noels L and Geuzaine C 2013 *J. Comput. Appl. Math.* **246** 243–50
[36] Henrotte F, Nicolet A and Hameyer K 2006 *COMPEL - Int. J. Comput. Math. Electr. Electron. Eng.* **25** 71–80
[37] Henrotte F, Steentjes S, Hameyer K and Geuzaine C 2014 *IEEE Trans. Magn.* **50** 333–6
[38] Preisach F 1935 *Z. Phys.* **94** 277–302
[39] Bertotti G 1992 *IEEE Trans. Magn.* **28** 2599–601
[40] Jiles D C and Atherton D L 1986 *J. Magn. Magn. Mater.* **61** 48–60
[41] Jacques K 2018 Energy-based magnetic hysteresis models—theoretical development and finite element formulations *PhD Thesis* Université de Liège
[42] Bergqvist A 1997 *Physica B* **233** 342–7
[43] Pike C 2003 *Phys. Rev. B* **68** 104424
[44] Escamez G, Sirois F, Tousignant M, Badel A, Granger C, Tixador P and Bruzek C E 2017 *Supercond. Sci. Technol.* **30** 034008
[45] Nikulshin Y, Wolfus S, Friedman A, Ginodman V, Grasso G, Tropeano M, Bovone G, Vignolo M, Ferdeghini C and Yeshurun Y 2018 *IEEE Trans. Appl. Supercond.* **28** 1–6